Terahertz conductivity of graphene on boron nitride

Ashley M. DaSilva, Jeil Jung, Shaffique Adam, and Allan H. MacDonald

Phys. Rev. B **92**, 155406 — Published 5 October 2015

DOI: 10.1103/PhysRevB.92.155406

THz conductivity of graphene on boron nitride

Ashley M. DaSilva,[1] Jeil Jung,[2] Shaffique Adam,[3,4] and Allan H. MacDonald[1]

[1] *Department of Physics, The University of Texas at Austin, Austin, Texas 78712-1192, USA*
[2] *Department of Physics, University of Seoul, Seoul 130-743, Korea*
[3] *Centre for Advanced 2D Materials and Department of Physics, National University of Singapore, 2 Science Drive 3, Singapore 117542*
[4] *Yale-NUS College, 16 College Ave West, Singapore 138527*

The conductivity of graphene on a boron nitride substrate exhibits features in the terahertz (THz) and infrared (IR) frequency regimes that are associated with the periodic moiré pattern formed by the weakly coupled two-dimensional materials. The THz and IR features are strongest when the two honeycomb lattices are orientationally aligned, and in this case are Pauli blocked unless the Fermi level is close to ±150 meV relative to the graphene sheet Dirac point. Because the transition energies between moiré bands formed above the Dirac point are small, *ac* conductivity features in n-doped graphene tend to be overwhelmed by the Drude peak. The substrate-induced band splitting is larger at energies below the Dirac point, however, and can however lead to sharp features at THz and IR frequencies in p-doped graphene. In this Letter we focus on the strongest few THz and IR features, explaining how they arise from critical points in the moiré-band joint density-of-states, and commenting on the interval of Fermi energy over which they are active.

Introduction:— Strong interactions between graphene sheets and light have motivated research aimed at potential graphene-based optoelectronic devices[1–5] operating in the terahertz (THz) and the infrared (IR) frequency regimes, a range of the electromagnetic spectrum that is important for imaging, sensing, and communications technologies.[6–10] The ability to tune carrier density in graphene using gate voltages[11] is a great advantage in most application possibilities.

The *ac* conductivity of a neutral graphene sheet[12–14] is nearly frequency-independent $\sigma_0 = \pi e^2/2h$; adding n or p type carriers transfers oscillator strength over the frequency interval $(0, 2\omega_F)$ which is Pauli blocked for interband transitions to a Drude peak of equal weight. When a graphene sheet is aligned with a hexagonal boron nitride substrate secondary Dirac points are induced by the substrate and, because they are gapped, lead to a large joint density-of-states for low-frequency optically active transitions. Like the interband conductivity of an isolated graphene sheet, the sharp conductivity features associated with these transitions can be turned off and on by adjusting the position of the Fermi level. (See Fig. 1). In this Letter we present a theory of the conductivity at Fermi level values close to secondary Dirac points.

Hexagonal boron nitride is a wide band gap semiconductor[15] with a hexagonal lattice structure and weakly coupled layers. Placing graphene on a hexagonal boron nitride substrate retains the high quality of graphene[16–18] while modifying its band structure and therefore its optical response. The substrate's pattern of negatively charged boron atoms and positively charged nitrogen atoms on opposite honeycomb sublattices alters the graphene π-band Hamiltonian. If the two honeycomb lattices had perfectly matched lattice constants and orientations, the primary effect of this interaction would be to simply to open a gap at the Dirac point.[19,20] However, the boron nitride lattice constant is about two percent larger than that of graphene and differences in orientation are typical in exfoliated samples,[17,21] leading to a more complex electronic structure. In nearly aligned layers, long-period moiré patterns[17,18,22] form and influence all physical properties. Experiments show that a gap opens at the Fermi level of neutral graphene sheets, with a value that is dependent on electron-electron interactions, and on strains induced by the lattice constant and orientation mismatch.[23–25] At perfect alignment (zero relative rotation angle between the graphene and boron nitride), the moiré wavelength is around 15 nm. In addition to the gap at charge neutrality, secondary gapped Dirac points appear[21,22,26–30] at Fermi energies corresponding to ±4 electrons per moiré period,

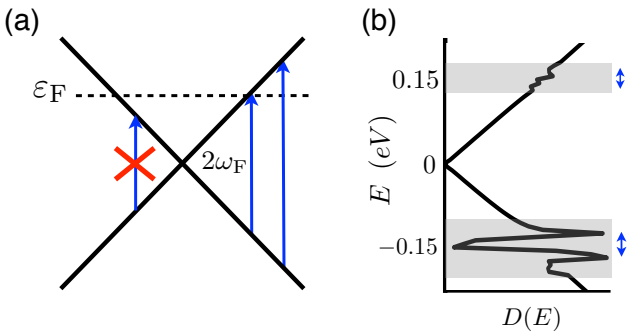

Figure 1. **Pauli blocking in bare graphene.** (a) This cartoon shows the Dirac cone of doped isolated graphene with a Fermi level ε_F given by the dashed line. Blue arrows represent interband transitions from the valence band to the conduction band. The middle arrow, with frequency $2\omega_F = 2\varepsilon_F/\hbar$, is at the minimum frequency for interband transitions. Below $2\omega_F$, transitions are not allowed due to the Pauli exclusion principle. (b) Density of states of aligned graphene on hBN. The shaded regions represent the locations of the substrate induced gapped Dirac cone replicas. The conductivity is strongly Fermi level dependent near these energies because of Pauli blocking.

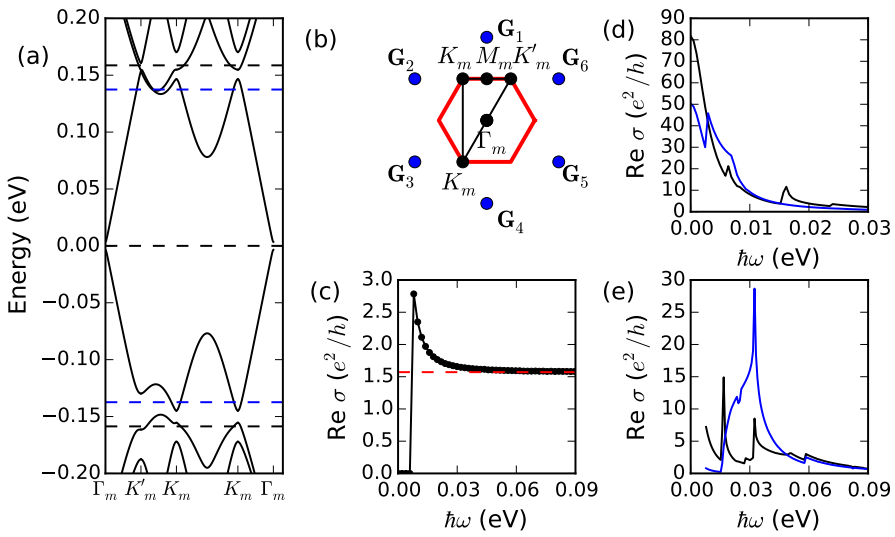

Figure 2. **Band structure and *ac* conductivity of graphene on boron nitride.** (a) Band structure of orientationally aligned graphene on boron nitride. The dashed lines show the Fermi levels for which the *ac* conductivity has been calculated. (b) Schematic picture of the moiré Brillouin zone, outlined in red. The bands are plotted along the black lines in momentum space. Blue dots represent the first shell of moireé reciprocal lattice vectors. (c) The *ac* conductivity when the Fermi level is at the Dirac point $\varepsilon_F = 0$. The red dashed line shows that $\sigma(\omega)$ approaches the bare graphene value $\sigma_0 = \pi e^2/2h$ at high frequencies. (d) The *ac* conductivity when the Fermi level is in the conduction band and near the secondary Dirac point with $\varepsilon_F = \hbar v G/\sqrt{3}$ (black) and near the secondary Dirac point with $\varepsilon_F = \hbar v G/2$ (blue). G is the magnitude of the moiré reciprocal lattice vectors in the first shell. (e) The *ac* conductivity when the Fermi level is in the valence band and near the secondary Dirac point with $\varepsilon_F = -\hbar v G/\sqrt{3}$ (black) and $\varepsilon_F = -\hbar v G/2$ (blue).

which corresponds in perfectly aligned graphene to Fermi levels $\sim \pm 150$ meV. This Fermi level scale is set by the moiré period, and can easily be reached by gating. The substrate interaction yields particle-hole asymmetry, and in particular leads to very different densities-of-states in conduction and valence bands.[22,27–29,31,32]

The *ac* conductivity is dominated by the intraband Drude peak and interband features associated with singularities in the joint density-of-states. It is therefore strongly affected by the band structure modifications induced by the boron nitride substrate. Previous work has highlighted the feasibility of using optical absorption to determine properties of the substrate interaction.[33,34] In this paper, we use a substrate interaction Hamiltonian[30] derived from *ab initio* electronic structure calculations to evaluate the *ac* conductivity of graphene on boron nitride. We focus on the case of perfect orientational alignment. In contrast to other substrates for which the *ac* conductivity in the THz regime is dominated by a broad intraband Drude peak, the moiré pattern formed by graphene on boron nitride sometimes induces sharp THz peaks due to transitions between Bloch bands formed by the moiré superlattice. The particle-hole asymmetry of the moiré Bloch bands is strongly reflected in the THz and IR conductivity which is always Drude-dominated when the Fermi level lies above the Dirac point, but is interband-dominated when the Fermi energy lies in a relatively narrow interval below the Dirac point. The qualitative change in THz and IR conductivity with Fermi energy suggests a potential mechanism for electrically tunable optical properties.

THz conductivity calculation:— We employ the moiré band Hamiltonian for graphene π-band electrons described in Ref.30 in which a local periodic substrate interaction term is added to the $\mathbf{k}\cdot\mathbf{p}$ continuum Dirac model of an isolated graphene sheet. The substrate interaction is extracted from *ab initio* electronic structure calculations[20,30] and is accurate for moiré patterns with spatial periods much larger than the graphene sheet lattice constant.[35] In previous work, we have used this approach to show how strains in the graphene lattice and the substrate together with electron-electron interactions control the size of the gap at the Fermi level of neutral graphene sheets.[30] We have also explained the subtle way in which substrate induced changes in carbon-site energies and hopping strengths combine to yield surprisingly strong particle-hole asymmetry that is manifested both in the density-of-states and in *dc* transport properties .[32]

The real part of the *ac* conductivity can be evaluated at zero temperature and frequency ω using the Kubo formula expression[14,32,36,37]

$$\mathrm{Re}\,\sigma(\omega) = \frac{\sigma(0)}{1+(\omega\tau)^2} + \frac{\pi e^2}{\hbar}\sum_{n,m\neq n\mathbf{k}} \frac{\Theta(\varepsilon_F-\varepsilon_{m,\mathbf{k}})-\Theta(\varepsilon_F-\varepsilon_{n,\mathbf{k}})}{\varepsilon_{n,\mathbf{k}}-\varepsilon_{m,\mathbf{k}}} \left|\left\langle n,\mathbf{k}\left|\frac{\partial H}{\partial \mathbf{k}}\right|m,\mathbf{k}\right\rangle\right|^2 \delta(\hbar\omega+\varepsilon_{n,\mathbf{k}}-\varepsilon_{m,\mathbf{k}}) \qquad (1)$$

where τ is taken to be the momentum relaxation time, ε_F is the Fermi energy, $\varepsilon_{n,\mathbf{k}}$ is the energy of moiré band n at wave vector $\mathbf{k}$, and $|n,\mathbf{k}\rangle$ is the eigenstate. The step functions, $\Theta(x)$, ensure that transitions occur only when one state is filled and one is empty, while the Dirac delta function $\delta(x)$ enforces energy conservation. The matrix elements can be simplified by noting that the Hamiltonian depends on $\mathbf{k}$ only through the continuum Dirac part, $\hbar v\mathbf{k}\cdot\tau$, where τ^α are Pauli matrices ($\alpha = x, y$).

The results of a calculation of the *ac* conductivity in which Eq. 1 was evaluated numerically are illustrated in Fig. 2, which also plots the moiré bands and summarizes the geometry of the moiré Brillouin zone. The plotted bands describe states near the microscopic K Dirac point and given eigenenergy as a function of momentum measured from that point in momentum space. The Hamiltonian near the microscopic K' Dirac point is related to the Hamiltonian at the K point by time reversal symmetry; the bands and energy eigenstates are therefore degenerate in the absence of a magnetic field. An external magnetic field breaks the time reversal symmetry, and the *ac* conductivity contributions from the two valleys will no longer be identical. In this paper, we consider only the case of zero magnetic field.

Because the moiré pattern is triangular, we choose to label symmetry points in the moiré band structure plots conventionally with subscript m, although all indicate points in momentum space close to the Brillouin-zone corner K of the microscopic reciprocal lattice. The low-energy electronic structure consists of moiré bands associated with each of graphene's two valleys. The Kramers partner of a moiré band state associated with one valley lies in the opposite valley. For this reason the moiré band structure of a particular valley is not time reversal invariant, allowing the energies at moiré K_m and K'_m points to be different. When the Fermi level is at the Dirac point a gap opens due to sublattice symmetry breaking. The conductivity is therefore zero for frequencies below the gap, peaks above the absorption threshold, and approaches the universal conductivity of isolated graphene $\sigma_0 = \pi e^2/2h$[14,38] at high frequencies. There is no transport gap at any Fermi level value in the conduction band, so there is always a significant contribution to the conductivity from the Drude term peaked at $\omega = 0$. Small features superimposed on the Drude peak appear at finite ω and are associated with the onset of interband transition channels as the frequency increases. In contrast to the case in the conduction band, for clean enough samples, there is a transport gap in the valence band when the hole density is four per moiré peirod. When the Fermi level lies in or just above or just below the moiré band edges (as shown in Figure 2) the Fermi surfaces are small, and so the Drude contribution remains smaller than in the conduction band case. Interband transitions are then dominant. Below we associate different peaks with transitions between moiré bands at different points in momentum space.

THz conductivity analysis:— In Fig. 3 we have separated the interband conductivity into contributions from pairs of moiré bands which cover energy intervals below the Dirac point energy. For each pair we have identified the dominant features, and associated them with transitions at or near high-symmetry points in the moiré Brillouin zone which are marked by arrows in the band structure panels of Fig. 3. First consider Fermi level $\varepsilon_F = \varepsilon_1 \equiv \hbar v G/\sqrt{3}$ at which all three interband transitions are active. We order the valence bands in reverse order of energy so that the first valence band is the one closest to the Dirac point in energy.

We see in Fig. 3 that the second subband is flatter over a wider region of momentum space than either the first or the third valence band. Accordingly third to first transitions make a smaller contribution to the interband conductivity than either third to second or second to first transitions. The two strongest features are a third to second transition from near the K_m, K'_m points with energy 0.017 eV (red in the right panel) and second to first transitions along the K_m, M_m line with energy 0.032 eV(purple in the left panel). All features can be identified with particular high symmetry points or lines in the moiré Brillouin zone, as shown by the matching colored arrows in the band structure plots. Generally speaking the strongest features are associated with interband transitions near the K_m and K'_m points in the moiré Brillouin zone. The top row of Figure 3 shows differences in band energy ΔE as a function of position in the moiré Brillouin zone as a contour plot. Up to a matrix element factor, the optical conductivity is proportional to the joint density of states. For transitions from the 2nd to 1st band ΔE has a saddle point at K_m which leads to a divergence in the joint density of states. In contrast, extrema in the transition energy yield jump discontinuities in the joint density of states[39] and weaker optical conductivity features. We note that in an experiment, the presence of impurities (which we have ignored for interband transitions) will broaden the features, and lead to a finite conductivity at saddle points.

The relatively small change in Fermi level to $\varepsilon_F = \varepsilon_2 \equiv \hbar v G/2$ leads to a very different conductivity profile. Because both the 2nd and 3rd bands are full, transitions between these two are forbidden, leading to a zero contribution from this pair of bands. The dominant feature becomes the 2nd to 1st band transitions at the K'_m point. This feature increases in strength as the Fermi level moves into the transport gap, and will decrease to zero as the Fermi level is moved into the first valence

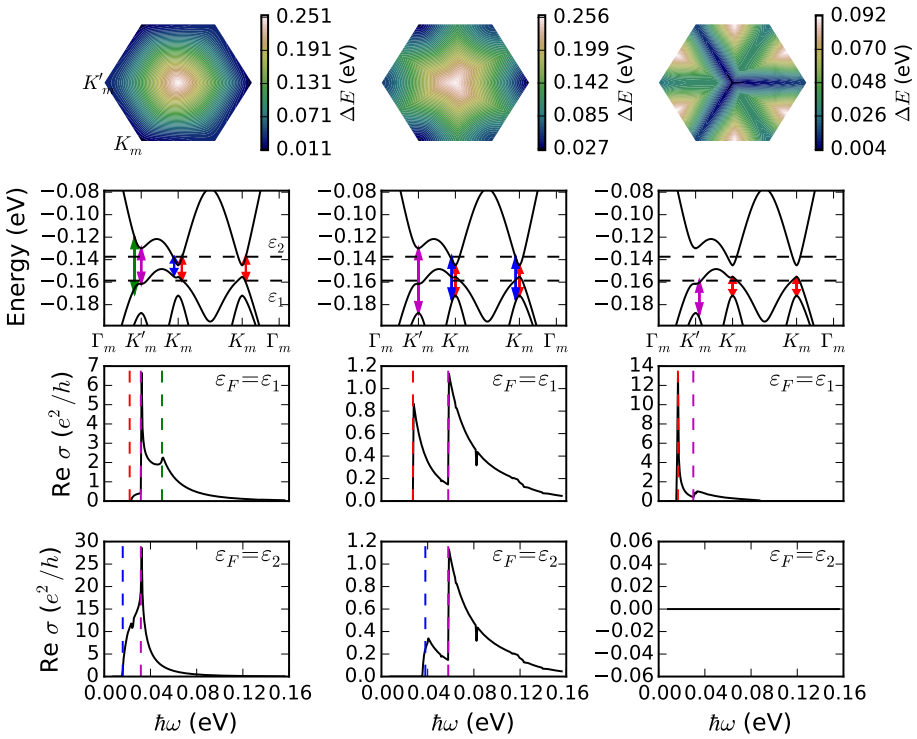

Figure 3. **Valence band conductivity features association with transitions at high symmetry points in the moiré Brillouin zone.** The interband transition energy (first row), band structure (second row) and conductivity (third and forth rows) for interband transitions between three pairs of valence bands. The left column corresponds to transitions from the second to first valence band; the middle column corresponds to transitions from the third to first valence band; and the right column corresponds to transitions from the third to second valence band. In the band structures (second row) dominant transitions have been identified with colored arrows, and their corresponding energies are marked as vertical dashed lines on the conductivity plots (third and fourth rows). The two Fermi energies at which calculations were performed, marked by black horizontal dashed lines on the band structure plots, are $\varepsilon_1 = -\hbar v G/\sqrt{3}$ and $\varepsilon_2 = -\hbar v G/2$. The third row corresponds to Fermi energy $\varepsilon_F = \varepsilon_1$, while the fourth row corresponds to Fermi energy $\varepsilon_F = \varepsilon_2$.

band. Note that this quite large change in the conductivity is seen over a relatively small change in Fermi level of ~ 20 meV.

For both Fermi levels, transitions from the 3rd to 1st bands are relatively weak. The reason for this is two fold. Firstly, the magnitude of the energy difference is larger. Since the conductivity is inversely proportional to this energy difference, this leads to a smaller conductivity. Secondly, as shown in the middle contour plot in Figure 3 the transition energies at both K_m and K'_m for this pair of bands are minima, not saddle points, and therefore do not lead to divergences in the conductivity. The contribution to conductivity due to these transitions are jump discontinuities, and have a relatively small magnitude compared to the saddle point divergences discussed above.

Although we have explicitly accounted for disorder in modeling the Drude peak in the ac conductivity, we have not accounted for its influence on the inter-moire-band features of primary interest. Provided that the disorder potential correlation length is shorter than the moire pattern period, its influence will simply be to endow the moire band Bloch states with a finite lifetime τ. All the interband features we calculate will therefore be broadened by $\sim \hbar/\tau$, and will be observable only if $\omega\tau$ is large. The moire pattern related THz conductivity features will therefore be observable only in graphene with a mobility larger than ~ 2000 cm^2/Vs.

Conclusions— We find that the conductivity of graphene on a boron nitride substrate is extremely sensitive to Fermi level. The system's particle-hole asymmetry is strongly manifested in the *ac* conductivity. For Fermi levels in the conduction band, the Drude peak dominates at low frequencies. For Fermi levels in the valence band, on the other hand, interband transitions dominate when the carrier density is close to four holes per moiré unit cell. All features in the *ac* conductivity are associated with transitions at high-symmetry points in the

moiré Brillouin zone which support critical points in the joint density of states. Depending on the Fermi level, transitions between the first and second moiré valence bands, or between the second and third bands, which have transition energy saddle points and associated divergent joint densities-of-states, dominate the total conductivity. These large and easily tunable changes in conductivity may be valuable for THz or IR applications.

Acknowledgements:— Work in Austin was supported by the Department of Energy, Office of Basic Energy Sciences under contract DE-FG02-ER45118 and by the Welch foundation under grant TBF1473. Work in Singapore was supported by the National Research Foundation of Singapore under its Fellowship programme (NRF-NRFF2012-01). We gratefully acknowledge the use of computational resources supplied by the Texas Advanced Computing Center.

[1] Farhan Rana, "Graphene Terahertz Plasmon Oscillators," IEEE Transactions on Nanotechnology **7**, 91–99 (2008).
[2] F. Bonaccorso, Z. Sun, T. Hasan, and A. C. Ferrari, "Graphene photonics and optoelectronics," Nature Photonics **4**, 611–622 (2010).
[3] Ashkan Vakil and Nader Engheta, "Transformation Optics Using Graphene," Science **332**, 1291–1294 (2011).
[4] Berardi Sensale-Rodriguez, Rusen Yan, Michelle M. Kelly, Tian Fang, Kristof Tahy, Wan Sik Hwang, Debdeep Jena, Lei Liu, and Huili Grace Xing, "Broadband graphene terahertz modulators enabled by intraband transitions," Nature Communications **3**, 780 (2012).
[5] Fangli Liu, Y. D. Chong, Shaffique Adam, and Marco Polini, "Gate-tunable coherent perfect absorption of terahertz radiation in graphene," 2D Materials **1**, 031001 (2014).
[6] B. B. Hu and M. C. Nuss, "Imaging with terahertz waves," Optics Letters **20**, 1716–1718 (1995).
[7] Michael C. Kemp, P. F. Taday, Bryan E. Cole, J. A. Cluff, Anthony J. Fitzgerald, and William R. Tribe, "Security applications of terahertz technology," (2003) pp. 44–52.
[8] Kodo Kawase, "Terahertz Imaging For Drug Detection And Large-Scale Integrated Circuit Inspection," Optics and Photonics News **15**, 34–39 (2004).
[9] Martin Koch, "Terahertz Technology:A Land to Be Discovered," Optics and Photonics News **18**, 20–25 (2007).
[10] A. Tang, N. Chahat, and E. Decrossas, "CMOS THz communication links for wireless applications: Where do they fit into mobile access and fixed access?" in *2014 39th International Conference on Infrared, Millimeter, and Terahertz waves (IRMMW-THz)* (2014) pp. 1–2.
[11] K. S. Novoselov, A. K. Geim, S. V. Morozov, D. Jiang, Y. Zhang, S. V. Dubonos, I. V. Grigorieva, and A. A. Firsov, "Electric Field Effect in Atomically Thin Carbon Films," Science **306**, 666–669 (2004).
[12] Feng Wang, Yuanbo Zhang, Chuanshan Tian, Caglar Girit, Alex Zettl, Michael Crommie, and Y. Ron Shen, "Gate-Variable Optical Transitions in Graphene," Science **320**, 206–209 (2008).
[13] Z. Q. Li, E. A. Henriksen, Z. Jiang, Z. Hao, M. C. Martin, P. Kim, H. L. Stormer, and D. N. Basov, "Dirac charge dynamics in graphene by infrared spectroscopy," Nature Physics **4**, 532–535 (2008).
[14] Tsuneya Ando, Yisong Zheng, and Hidekatsu Suzuura, "Dynamical Conductivity and Zero-Mode Anomaly in Honeycomb Lattices," Journal of the Physical Society of Japan **71**, 1318–1324 (2002).
[15] Kenji Watanabe, Takashi Taniguchi, and Hisao Kanda, "Direct-bandgap properties and evidence for ultraviolet lasing of hexagonal boron nitride single crystal," Nature Materials **3**, 404–409 (2004).
[16] C. R. Dean, A. F. Young, I. Meric, C. Lee, L. Wang, S. Sorgenfrei, K. Watanabe, T. Taniguchi, P. Kim, K. L. Shepard, and J. Hone, "Boron nitride substrates for high-quality graphene electronics," Nature Nanotechnology **5**, 722–726 (2010).
[17] Jiamin Xue, Javier Sanchez-Yamagishi, Danny Bulmash, Philippe Jacquod, Aparna Deshpande, K. Watanabe, T. Taniguchi, Pablo Jarillo-Herrero, and Brian J. LeRoy, "Scanning tunnelling microscopy and spectroscopy of ultra-flat graphene on hexagonal boron nitride," Nature Materials **10**, 282–285 (2011).
[18] Regis Decker, Yang Wang, Victor W. Brar, William Regan, Hsin-Zon Tsai, Qiong Wu, William Gannett, Alex Zettl, and Michael F. Crommie, "Local Electronic Properties of Graphene on a BN Substrate via Scanning Tunneling Microscopy," Nano Letters **11**, 2291–2295 (2011).
[19] Gianluca Giovannetti, Petr A. Khomyakov, Geert Brocks, Paul J. Kelly, and Jeroen van den Brink, "Substrate-induced band gap in graphene on hexagonal boron nitride: Ab initio density functional calculations," Physical Review B **76**, 073103 (2007).
[20] Jeil Jung, Arnaud Raoux, Zhenhua Qiao, and A. H. MacDonald, "Ab initio theory of moir superlattice bands in layered two-dimensional materials," Physical Review B **89**, 205414 (2014).
[21] Carmine Ortix, Liping Yang, and Jeroen van den Brink, "Graphene on incommensurate substrates: Trigonal warping and emerging Dirac cone replicas with halved group velocity," Physical Review B **86**, 081405 (2012).
[22] Matthew Yankowitz, Jiamin Xue, Daniel Cormode, Javier D. Sanchez-Yamagishi, K. Watanabe, T. Taniguchi, Pablo Jarillo-Herrero, Philippe Jacquod, and Brian J. LeRoy, "Emergence of superlattice Dirac points in graphene on hexagonal boron nitride," Nature Physics **8**, 382–386 (2012).
[23] B. Hunt, J. D. Sanchez-Yamagishi, A. F. Young, M. Yankowitz, B. J. LeRoy, K. Watanabe, T. Taniguchi, P. Moon, M. Koshino, P. Jarillo-Herrero, and R. C. Ashoori, "Massive Dirac Fermions and Hofstadter Butterfly in a van der Waals Heterostructure," Science **340**, 1427–1430 (2013).
[24] L. A. Ponomarenko, R. V. Gorbachev, G. L. Yu, D. C. Elias, R. Jalil, A. A. Patel, A. Mishchenko, A. S. Mayorov, C. R. Woods, J. R. Wallbank, M. Mucha-Kruczynski, B. A. Piot, M. Potemski, I. V. Grigorieva, K. S. Novoselov, F. Guinea, V. I. Falko, and A. K. Geim, "Cloning of Dirac fermions in graphene superlattices," Nature **497**, 594–597 (2013).
[25] C. R. Woods, L. Britnell, A. Eckmann, R. S. Ma, J. C. Lu,

H. M. Guo, X. Lin, G. L. Yu, Y. Cao, R. V. Gorbachev, A. V. Kretinin, J. Park, L. A. Ponomarenko, M. I. Katsnelson, Yu N. Gornostyrev, K. Watanabe, T. Taniguchi, C. Casiraghi, H.-J. Gao, A. K. Geim, and K. S. Novoselov, "Commensurate-incommensurate transition in graphene on hexagonal boron nitride," Nature Physics **10**, 451–456 (2014).

[26] Cheol-Hwan Park, Li Yang, Young-Woo Son, Marvin L. Cohen, and Steven G. Louie, "New Generation of Massless Dirac Fermions in Graphene under External Periodic Potentials," Physical Review Letters **101**, 126804 (2008).

[27] M. Kindermann, Bruno Uchoa, and D. L. Miller, "Zero-energy modes and gate-tunable gap in graphene on hexagonal boron nitride," Physical Review B **86**, 115415 (2012).

[28] J. R. Wallbank, A. A. Patel, M. Mucha-Kruczynski, A. K. Geim, and V. I. Fal'ko, "Generic miniband structure of graphene on a hexagonal substrate," Physical Review B **87**, 245408 (2013).

[29] M. Mucha-Kruczynski, J. R. Wallbank, and V. I. Fal'ko, "Heterostructures of bilayer graphene and h-BN: Interplay between misalignment, interlayer asymmetry, and trigonal warping," Physical Review B **88**, 205418 (2013).

[30] Jeil Jung, Ashley M. DaSilva, Allan H. MacDonald, and Shaffique Adam, "Origin of band gaps in graphene on hexagonal boron nitride," Nature Communications **6**, 6308 (2015).

[31] Pilkyung Moon and Mikito Koshino, "Electronic properties of graphene/hexagonal-boron-nitride moir superlattice," Physical Review B **90**, 155406 (2014).

[32] Ashley M. DaSilva, Jeil Jung, Shaffique Adam, and Allan H. MacDonald, "Transport and particle-hole asymmetry in graphene on boron nitride," Physical Review B **91**, 245422 (2015), arXiv: 1503.04312.

[33] D. S. L. Abergel, J. R. Wallbank, Xi Chen, M. Mucha-Kruczynski, and Vladimir I. Fal'ko, "Infrared absorption by graphenehBN heterostructures," New Journal of Physics **15**, 123009 (2013).

[34] Zhiwen Shi, Chenhao Jin, Wei Yang, Long Ju, Jason Horng, Xiaobo Lu, Hans A. Bechtel, Michael C. Martin, Deyi Fu, Junqiao Wu, Kenji Watanabe, Takashi Taniguchi, Yuanbo Zhang, Xuedong Bai, Enge Wang, Guangyu Zhang, and Feng Wang, "Gate-dependent pseudospin mixing in graphene/boron nitride moire superlattices," Nature Physics **10**, 743–747 (2014).

[35] R. Bistritzer and A. H. MacDonald, "Moir\'e butterflies in twisted bilayer graphene," Physical Review B **84**, 035440 (2011).

[36] V. P. Gusynin, S. G. Sharapov, and J. P. Carbotte, "ac conductivity of graphene: from tight-binding model to 2+1-dimensional quantum electrodynamics," International Journal of Modern Physics B **21**, 4611–4658 (2007).

[37] L. A. Falkovsky and A. A. Varlamov, "Space-time dispersion of graphene conductivity," The European Physical Journal B **56**, 281–284 (2007).

[38] R. R. Nair, P. Blake, A. N. Grigorenko, K. S. Novoselov, T. J. Booth, T. Stauber, N. M. R. Peres, and A. K. Geim, "Fine Structure Constant Defines Visual Transparency of Graphene," Science **320**, 1308–1308 (2008).

[39] Daniela Dragoman and Mircea Dragoman, *Optical Characterization of Solids* (Springer, 2002).